small methods
www.small-methods.com

Nozzle-Free Printing of CNT Electronics Using Laser-Generated Focused Ultrasound

Sarah Seva, Benjamin Rorem, Karthik Chinnathambi, David Estrada, L. Jay Guo, and Harish Subbaraman**

Printed electronics have made remarkable progress in recent years and inkjet printing (IJP) has emerged as one of the leading methods for fabricating printed electronic devices. However, challenges such as nozzle clogging, and strict ink formulation constraints have limited their widespread use. To address this issue, a novel nozzle-free printing technology is explored, which is enabled by laser-generated focused ultrasound, as a potential alternative printing modality called Shock-wave Jet Printing (SJP). Specifically, the performance of SJP-printed and IJP-printed bottom-gated carbon nanotube (CNT) thin film transistors (TFTs) is compared. While IJP required ten print passes to achieve fully functional devices with channel dimensions ranging from tens to hundreds of micrometers, SJP achieved comparable performance with just a single pass. For optimized devices, SJP demonstrated six times higher maximum mobility than IJP-printed devices. Furthermore, the advantages of nozzle-free printing are evident, as SJP successfully printed stored and unsonicated inks, delivering moderate electrical performance, whereas IJP suffered from nozzle clogging due to CNT agglomeration. Moreover, SJP can print significantly longer CNTs, spanning the entire range of tube lengths of commercially available CNT ink. The findings from this study contribute to the advancement of nanomaterial printing, ink formulation, and the development of cost-effective printable electronics.

1. Introduction

Over the last decade, electronics have undergone a transformation from their traditional rigid form factor to flexible, bendable, stretchable, and lightweight printable forms to conform to or wrap around objects,[1–5] thanks to the significant advancements in the field of printed electronics. Recently, there has been an increasing adoption of printed electronics technologies and their integration with established electronics. This integration takes the form of flexible hybrid electronic (FHE) systems, which play a vital role in the development of the internet-of-things (IoT) and wearable technology.[6,7] Printed electronics have unlocked many applications that cannot be envisioned with rigid components. These applications include wearable computing,[6–10] flexible optoelectronics,[11] personal health monitoring systems,[12] environmental monitoring,[13] radio-frequency identification,[14–18] sensors,[19] smartwatches, electronic tattoos, and energy harvesters.[20–25] These applications have

S. Seva
Electrical and Computer Engineering
Boise State University
1910 W University Drive, Boise, ID 83725, USA

B. Rorem, L. J. Guo
Applied Physics
University of Michigan
Ann Arbor, MI 48109, USA
E-mail: guo@umich.edu

K. Chinnathambi, D. Estrada
Micron School of Materials Science and Engineering
Boise State University
1910 W University Drive, Boise, ID 83725, USA

D. Estrada
Center for Advanced Energy Studies
Idaho National Laboratory
Idaho Falls, ID 83415, USA

L. J. Guo
Department of Electrical Engineering and Computer Science
University of Michigan
Ann Arbor, MI 48109, USA

H. Subbaraman
School of Electrical Engineering and Computer Science
Oregon State University
110 SW Park Terrace Pl, Corvallis, OR 97331, USA
E-mail: harish.subbaraman@oregonstate.edu

The ORCID identification number(s) for the author(s) of this article can be found under https://doi.org/10.1002/smtd.202301596

DOI: 10.1002/smtd.202301596

been made possible for several reasons. First, printed electronics are cost-effective due to their additive manufacturing process, which operates at low temperatures or without the need for vacuum systems.[22,23] Second, printed electronics are compatible with various types of substrates, allowing for the development of flexible and large-area hybrid electronic systems.[24] Third, printed electronic sensors have demonstrated functionality across a diverse range of applications, including pressure sensing,[25,26] biosensing,[27] temperature sensing,[28] and others.[29–32] One of the most attractive features of printed electronics is their ability to facilitate electronic sensors and systems that are compatible with the high-throughput, low-cost manufacturing demands of the IoT.

Among the widely used print modalities,[6,33] inkjet printing,[28] and aerosol jet printing[32] possess unique features that enable diverse applications. However, they are limited by nozzle clogging.[34,35] Nozzle clogging can occur for various reasons, such as agglomeration and sedimentation due to van der Waals forces,[10–12] the large lateral dimension of the nanomaterials, especially the longer dimension of 1D nanomaterials,[36] and solvent evaporation at the nozzles.[14] To overcome these challenges, extensive research efforts have been undertaken, utilizing various methods such as nanomaterial dispersion using sidewall functionalization and organic solvents, but with associated challenges.[37] Process-induced defects related to ink formulation, for example, can result in the shortening of one dimensional (1D) material length and damage to the tube walls, limiting the printed material electrical performance.[13,35,38,39]

A novel nozzle-free printing technology, namely Shock-wave Jet Printing (SJP), has shown promise in addressing several issues in the material printing industry.[40,41] This technology achieves high-speed liquid microjetting through a nonthermal process, using a focused acoustic pulse less than 100 ns, thus eliminating the need for nozzles. These acoustic waves are excited by a pulsed Nd:YAG laser beam and are geometrically focused using a photoacoustic lens. To explore the potential of the nozzle-free SJP system for printed electronics applications, we printed carbon nanotube (CNT)-based back-gated transistors with SJP and compared them to the conventional nozzle-based inkjet (IJP) printed CNT transistor devices. To enable direct comparison between the printing technologies, only the CNT channel was printed using the two different methodologies, while the back-gated transistor structures with a photolithographically defined source and drain were fabricated on a low-resistance silicon wafer with 90 nm top oxide layer (dielectric).

From the comparative study of SJP-printed CNT channel in TFT to IJP, optimized SJP CNT-TFTs show promising transistor performance, surpassing IJP devices in terms of maximum field effect mobility, and on/off ratio. Notably, for a channel width of 300 µm and channel lengths varying from 2 to 300 µm, IJP required ten print passes (with only the 2 µm device functioning after five passes), whereas SJP technology achieved functional transistors across all channel lengths with just a single pass. To analyze the impact of the IJP nozzle, unsonicated ink, stored for several months with sporadic clots of tubes, was used, leading to immediate nozzle clogging in the IJP process. In contrast, the nozzle-free SJP process enabled printed devices with satisfactory transistor performance. This alleviation of sonication dependence for CNT ink is a direct result of nozzle-free, high-speed liquid microjetting. This also minimizes CNT damage, resulting in longer tube lengths spanning the entire length range of the commercially available CNT ink and improved device performance in terms of threefold maximum field effect mobility. Additionally, SJP is expected to be more cost-effective when considering factors such as sonication, printing passes, and ink volume used.

2. Nozzle-Based and Nozzle-Free Printing Technology

In the widely used drop-on-demand (DoD) piezoelectric inkjet printing (IJP) technology, an extremely repeatable formation of small fluid droplets is directed to a specific location with high accuracy, enabled by computer-aided design (CAD) image-to-print patterns[42] with specific requirements for microelectronic research. In this printer, a piezoelectric actuator guided by a voltage waveform is used to displace ink by creating a pressure wave that travels to the nozzle and ejects ink droplets, as reported in the literature.[43–48] Although IJP is simple and widely used for successful printing of nanomaterials, several challenges appear – the ink must maintain low surface tension and low viscosity while incorporating nanomaterials to ensure their dispersion and prevent nanomaterial flocculation. Nanomaterials like CNTs can easily agglomerate and sediment due to the van der Waals forces among the tubes, eventually clogging the inkjet nozzle.[42–53] To alleviate this issue, extensive research efforts have explored various methods of CNT dispersion, including surface functionalization for use in organic solvents, and dispersants in the case of water-based ink. Although surface functionalization aids in dispersion, it may negatively impact CNT conductivity.[53] Organic solvents can act as dispersants and adsorb onto the carbon nanotube surface through hydrophobic interactions, countering the strong van der Waals forces between the nanotubes[53] and providing an effective alternative for surface functionalization. However, organic solvents have additional challenges. They limit CNT concentration to ≈ 0.1 mg mL^{-1},[54] causing ink preparation issues due to organic solvent volatility. Evaporation in ink cartridges can eventually cause nozzle clogging. To avoid nozzle clogging mass loading has to be limited,[51] which in turn requires an increase in the number of print passes. Even after selecting proper compounds, sonication using high frequency vibrations is required to separate carbon nanotubes to avoid agglomeration, however, this is coupled with the downside of enhanced defects in the CNTs, limiting the final TFT performance.

As nozzle clogging problems are frequently encountered in inkjet printing, especially for 1D nanomaterials with longer dimension,[38] stringent conditions, such as low precipitation and small particle sizes are required in ink formulation. For example, the diameter of Samba cartridge and silicon nozzle opening used in the Dimatix inkjet printer are 18.2 µm[55] and 21.5 µm,[56] respectively. A rule of thumb for this type of nozzle-based printer is that it can print 1/50th of its nozzle size, which in this case is ≈0.43 µm. To fabricate back-gated CNT-TFT with device schematic shown in **Figure 1a**, we used 99.9% pure semiconducting single-walled carbon nanotube (S-SWCNT) (NanoIntegris) with a wide length range of 300–5 µm, as shown by the histogram in Figure S1 (Supporting information).[57] With a maximum printable length limitation of 430 nm, more than 75% CNTs are estimated to be broken. Since mass-loading and

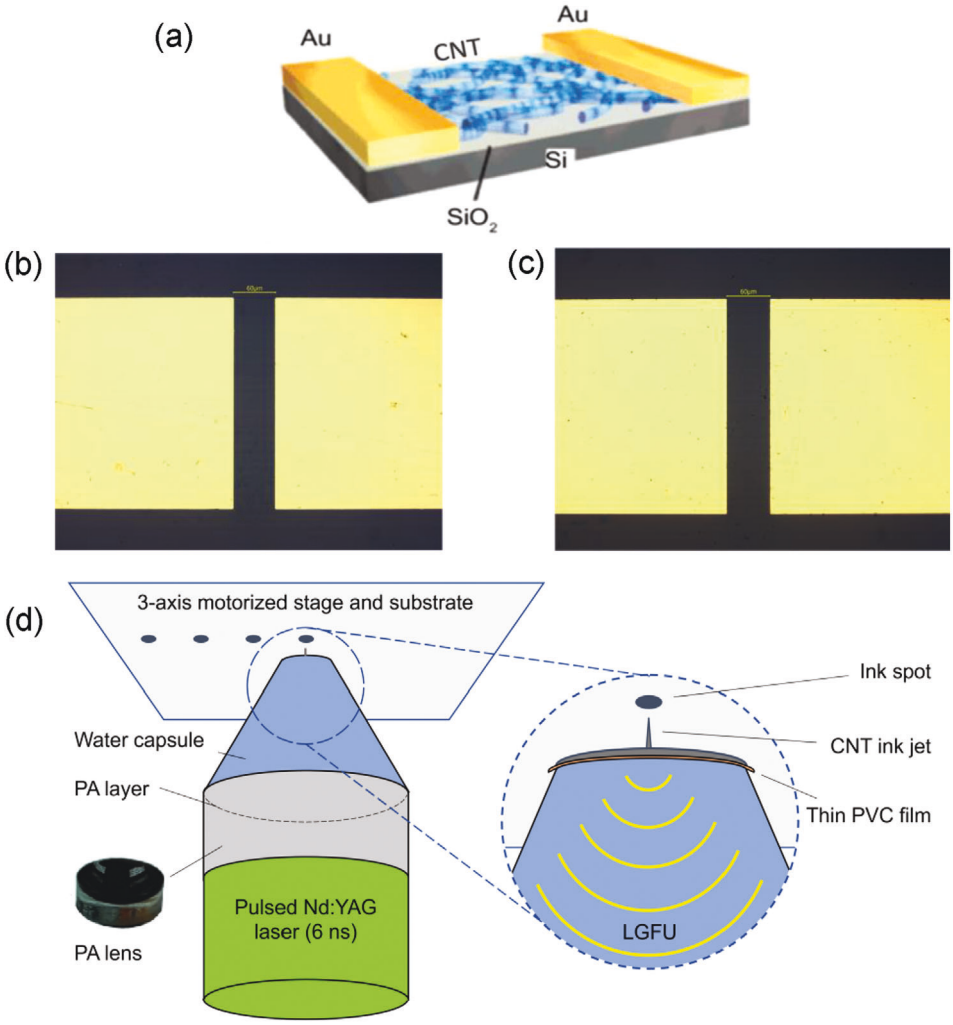

Figure 1. a) CNT transistor schematic, optical image of printed CNT channel by b) IJP and c) SJP between two Au electrodes separated by 60 microns on SiO_2/Si substrate with devices ready for electrical characterization, respectively, d) Schematic of the SJP setup. A pulsed laser illuminates a plano-concave photoacoustic (PA) lens which converts the light pulses (6 ns) to focused acoustic pulses (<100 ns). The acoustic pulses traverse water and a thin PVC membrane to focus at the air-ink interface. At the interface, the acoustic negative pressure exceeds the nucleation threshold of water, producing microcavities and microjets. A heated substrate, held by a three-axis motorized stage, is placed in the jet path to deposit ink spots and patterns.

material-size have been limited due to clogging of the printhead nozzle, alternative solutions have been pursued, including nozzle replacement.[38,58–63] To address this challenge, a nozzle-free printing technology is highly desirable for CNT-TFT printing.

While promising demonstrations of nozzle-free jetting schemes have been reported,[61–64] realizing practical applications is challenging for multiple reasons. Such challenges include slow speed,[62] uncontrolled high-speed jets, and laser-induced spherical bubble-based jetting requires optically transparent liquid and thermally stable materials to avoid high-temperature annealing-induced material property changes.[64,65] To accommodate these requirements, Guo et al developed a nozzle-free, high-speed liquid microjetting method based on a nonthermal process.[40,41] This previously reported method utilizes a short focused acoustic pulse (<100 ns) generated by a CNT photoacoustic lens capable of focusing to a spot the size of ≈ 100 µm. By creating a high negative pressure amplitude that exceeds the homogeneous nucleation threshold of water, high-speed jets (up to 200 m s^{-1})[40] are induced at the air-water interface through cavitation in water. The jet height is controlled by the magnitude of the impinged pressure wave, as well as the proximity of the focal point to the surface of the ink. Figure 1d illustrates the experimental setup for liquid jetting and photoacoustic (PA) generation. In this setup, liquid jets are created by focusing acoustic waves on the air–water interface from the water side. In this setup, the maximum jet height reaches 500 µm, so the working distance is set near 250 µm to keep the translating substrate comfortably within the jet's reach. The acoustic waves are produced using a transparent plano-concave lens coated with a carbon black composite material (referred to as PA lens hereafter). This carbon black coating, unlike the previously mentioned CNT lens, offers cost-effective and straightforward application while still producing efficient light-to-sound energy conversion and robust microjets. The

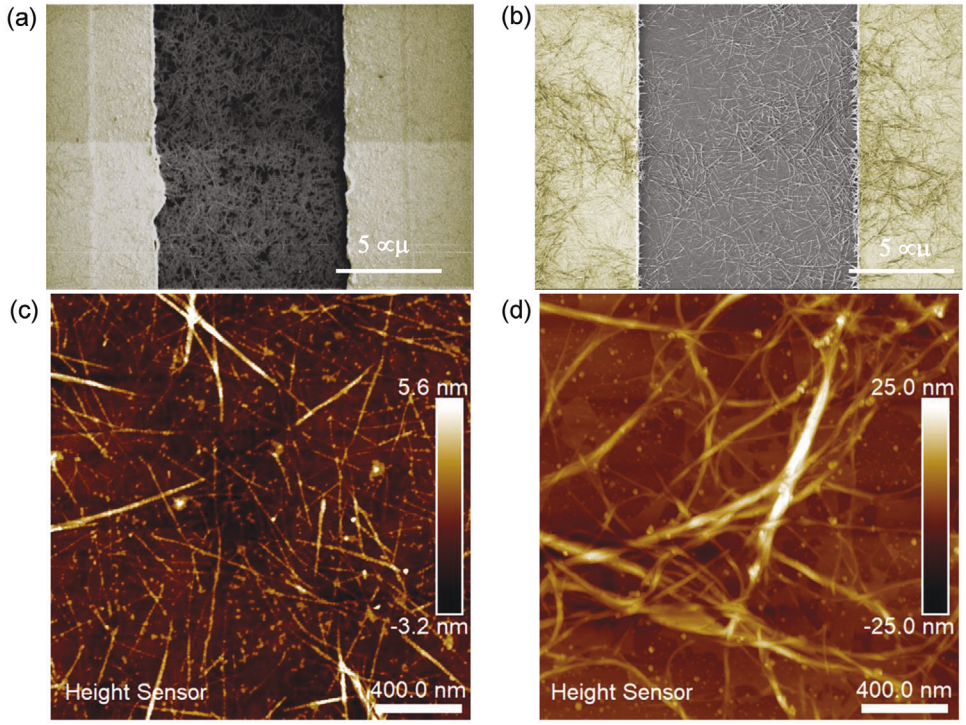

Figure 2. SEM image of printed CNT channel by a) IJP and b) SJP between Au electrodes (false colored) on SiO_2/Si substrate showing uniform coverage. Scale bar is 5 μm for both SEM images. AFM images of c) IJP 10-pass, and d) SJP 1-pass, printed devices showing only few CNTs can connect source and drain by SJP.

carbon black composite consists of soot particles deposited by flame synthesis and embedded in polydimethylsiloxane (PDMS) elastomer. The composite efficiently converts incident optical energy into heat that is rapidly transferred to the surrounding PDMS due to its high thermal expansion coefficient. The acoustic waves, excited by a pulsed Nd:YAG laser beam (Continuum, Surelite I-20, $\lambda = 532$ nm, pulse width = 6 ns), are geometrically focused following the curvature of the PA lens with a focal length of ≈ 5.5 mm. This is called laser-generated focused ultrasound (LGFU). The pressure pulse has a pulse width of less than 100 ns and a negative pressure amplitude exceeding 20 MPa in bulk water. To ensure minimal attenuation of the acoustic pulses, a water capsule is placed above the PA lens. Although the water capsule appears like a nozzle, any geometry is valid as long as the ultrasound is unimpeded. A cone is used in the SJP system to reduce water and ink consumption. Just below the focal point (≈1 mm), a thin PVC film separates the water and ink, preventing mixing while allowing the acoustic pulse to focus at the air-ink interface. A more comprehensive understanding of the experimental setup and jetting process visualization can be found in.[40,41] SJP is able to print liquids and solid particles nearing 100 μm due to its nozzle-free nature and forceful ejection mechanism. The resolution of water-based ink printed onto glass is 20–30 microns.[40] Functionalization of the surface and slower print speed will decrease the resolution as the ink spreads out. For IJP, a few micrometer size features have been achieved by employing high droplet resolutions of ink volume in picoliter enabled by various numbers of nozzles.[66,67] In the case of AJP, it achieved a resolution of 16 μm wide CNT lines on the flexible polyimide substrate by exploiting self-assembled and aligned CNT twin-lines as originated from the coffee-ring effect.[68] The device schematic, representative optical images for IJP and SJP printed devices, are shown in Figure 1a–c, respectively. The device fabrication process flow, and device layout pattern are depicted in Figure S2a,b (Supporting information), respectively. Details of sample photolithographically patterning, contact metallization, surface preparation for printing, and post print processing are described in the methods section.

3. Comparison of IJP and SJP Printed Devices

Figure 2a,b shows scanning electron microscopy (SEM) images of IJP and SJP printed CNT channel devices, respectively, the channel areas highlight uniform coverage of random CNT networks. Although the same ink is used for printing, there is a distinct difference between the CNT films printed by these two methods. The IJP printed device shows uniform coverage across the channel but requires 10 printing passes to achieve functional devices for 2–300 μm channel length and 300 μm width. The SJP printed device showed thinly dispersed CNTs, which require only one printing pass for the same channel dimensions to achieve functional TFTs. IJP printed CNTs are smaller in length (consistent with the earlier estimate based on the nozzle size), therefore requiring an increased number of printing passes to form fully connected and conducting percolating paths from source to drain. The 10 pass-printing also results in a much denser CNT network, i.e., more CNT consumption to achieve functional TFT. Although the printed CNT devices are bottom contacted, the

IJP-printed CNTs overlapping with metal contacts are not clearly visible due to small tube lengths and a dense network. On the other hand, SJP-printed CNTs are much longer thanks to its nozzle-free nature, as seen in the SEM image. They span a longer distance between the gold electrodes, forming sufficient percolating conduction paths to make functional devices by just a single printing pass. Similar observations are drawn from AFM images for IJP and SJP printed CNT channels shown in Figure 2c,d, respectively. Due to the denser CNT network, a surface roughness of 1.44 nm was observed for IJP compared to 2.8 nm for SJP printed devices. Both microscopy methods show a lower density of CNTs for SJP devices. Since the mobility depends on the CNT coverage, a python script was used to estimate total coverage. This analysis and the subsequent mobility values are shown later.

The I–V measurements show the effectiveness of the SJP printing. For the IJP-printed devices, it was observed that no semiconducting channel formed between source and drain electrodes for one and five printing passes, with the exception of the 2 µm channel-length device printed with five passes. This is because CNTs are shortened by the size of the nozzle. In contrast, SJP printing was able to produce functional transistors for the entire range of channel length from 2 to 300 µm with just one printing pass. Transistor transfer characteristics, represented as drain current (I_d) versus gate voltage (V_g), were obtained for the fabricated CNT-TFTs by applying gate voltages from −20 to 20 V to the heavily doped silicon substrate used as the global back gate, with a drain bias (V_d) of 1 V. Mobility of the devices was extracted using the equation, $\mu = \frac{g_m L}{W C_{ox} V_d}$ during the forward sweep (i.e., −20–20 V), with the parallel plate capacitor approximation. Here, g_m is the peak transconductance (dI_d/dV_g) obtained from the forward sweep of the transfer curve for each device. L is the channel length, W is the channel width, and C_{ox} is the oxide capacitance per unit area (ϵ_{ox}/t_{ox}). It is worth noting that parallel plate capacitance underestimates mobility (µ), particularly for low-density CNT networks where a fraction of the channel region is not covered by any CNTs. Conversely, forward sweep DC measurement overestimates mobility compared to reverse sweep and pulsed measurement due to hysteresis in transfer characteristics, which is attributed to charge trapping by surrounding water molecule or charge injection into dielectric substrate.[69] However, parallel plate capacitance and forward sweep-based field effect mobility extraction provide a convenient way to make direct comparisons with other reported results in the literature.[70,71] While direct measurement of the gate capacitance of CNT TFTs could yield a more accurate estimation of mobility, [72–74] it introduces additional complexities.

To compare the electrical performance of IJP and SJP printed CNT-TFTs, we investigated transfer characteristics and I_d–V_d family plots. **Figure 3a** exhibits representative transfer characteristics for inkjet and SJP devices with a channel dimension of 60 µm in length and 300 µm in width. The presence of hysteresis in the IJP and the SJP transfer characteristics is evident, which is typically attributed to charge trapping by surrounding water molecules or charge injection into the dielectric substrate.[71] While both devices exhibit good gate modulation, IJP devices demonstrate approximately twice the current compared to SJP-printed CNT-TFTs, as shown in Figure 3c,d, respectively. Here, V_g varies from −16.0 to −2.0 V in 2.0 V steps, while V_d varies from 0.0 to −12.0 V. The drain current values for IJP printed devices are two times higher than that of SJP in the I_d-V_d family plot under back gate bias of −16.0 V, similar to observations from the transfer characteristics. Such behavior can be attributed to denser CNT network and higher junction density as originated from multiple IJP pint passes. Furthermore, the I_d-V_d plots demonstrate that the drain current saturates at a lower V_d magnitude for IJP compared to SJP. For the IJP and SJP devices with a 60 µm channel length in Figure 3a, the extracted mobilities are ≈23 and ≈12 $cm^2\ V^{-1}\ s^{-1}$, respectively, with I_{ON}/I_{OFF} in the 10^2 and 10^3 orders of magnitude, respectively. However, it is essential to consider the difference in CNT density observed in Figure 2 while comparing transistor electrical performance metrics, such as extracted field effect mobility, between the two print modalities. To provide a fair comparison, CNT surface coverage is extracted for both cases, and mobility values are corrected based on the coverage.[75–77]

Using a Python script-based surface coverage analysis, we differentiated CNT-covered areas from SiO_2. IJP exhibited over 90% surface coverage, compared to only 32% for SJP (Images are included in the Supporting Information, Figure S3, Supporting information). This significant difference in surface coverage is expected to influence the field effect mobility of the devices, given that it affects the channel width in the equation $\mu = \frac{g_m L}{W C_{ox} V_d}$. The mobility values are scaled in proportion to the surface area coverages. IJP surface area coverage can be approximated as ≈100%, while SJP covers only about one-third of that. Accordingly, the effective channel width for SJP is corrected by this ratio, raising the SJP mobility values by the same factor. After mobility correction, for IJP and SJP devices with a 60 µm channel length, as shown in Figure 3a, the extracted mobilities are ≈23 and ≈36 $cm^2\ V^{-1}\ s^{-1}$, respectively. This is reasonable considering that the nozzle-free SJP preserves the original length of the CNTs, requiring fewer cross-connections of CNT strands. This aspect can be further verified by the maximum mobility achieved from SJP printed device, ≈135 $cm^2\ V^{-1}\ s^{-1}$, while for the same channel length, IJP printed device reached mobility of ≈22 $cm^2\ V^{-1}\ s^{-1}$. The I_{ON}/I_{OFF} are in the 10^3 and 10^5 orders of magnitude, respectively (transfer characteristics are shown in supporting document Figure S4 (Supporting information) for IJP and SJP devices with a 300 µm channel length).

To assess the impact of nozzles, we used unsonicated ink that had been stored for several months and formed sporadic clots of tubes. In the case of IJP, this stored ink, with clots and without sonication, caused nozzle clogging. SJP-printed devices exhibited satisfactory device performance, as shown in the transfer characteristics and I_d–V_d family plot in Figure 3b,e, respectively. These devices achieved a mobility of 10.8 $cm^2\ V^{-1}\ s^{-1}$ and an I_{ON}/I_{OFF} of ≈10^6, which are acceptable for printed electronic applications. Although unsonicated ink was successfully printed with SJP, lots of CNT clots were present in the ink without filtration. Clotted CNTs might have formed pseudo-isolated CNT channels similar to nano-meshing[78,79] or strip patterning[79,80] reported previously. After nanomesh formation,[78,79] a similar decrease in on- and off-current, increase in on/off ratio, and increase in transconductance were observed. Subsequently, reducing the separation between nanoholes increases the on/off ratio up to six orders of magnitude. This is attributed to a reduction in the probability of metallic subnetworks bridging the source

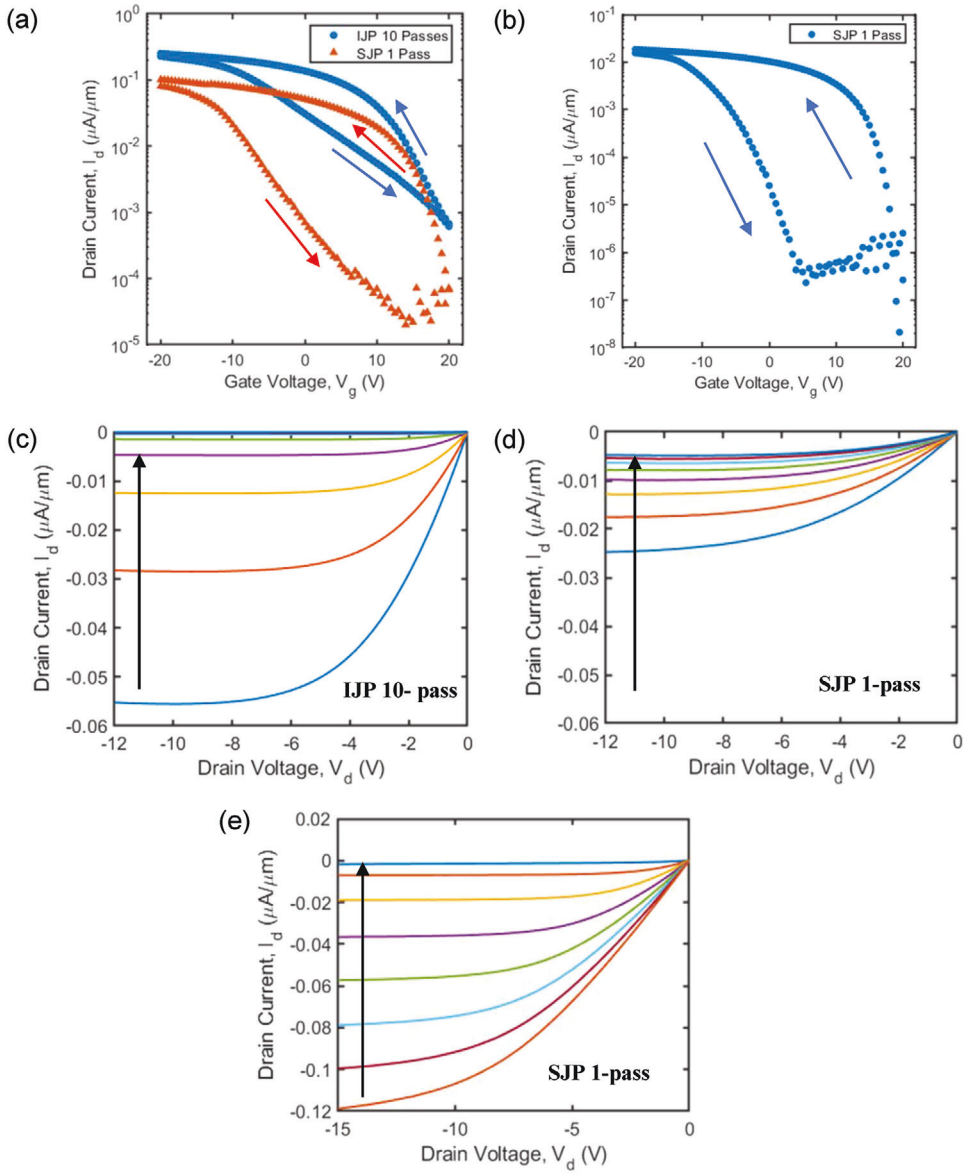

Figure 3. Transistor transfer characteristics obtained for the fabricated CNT-TFT for drain bias V_d = 1 V. a) Blue is IJP- and orange is SJP-printed device with sonicated ink for L = 60 µm and W = 300 µm. b) Similar plot for SJP printed CNT-TFT with unsonicated ink for drain bias V_d = 1 V, L = 80 µm and W = 300 µm. Similar printing attempt in IJP was unsuccessful due to nozzle clogging. I_d–V_d family plot for c) IJP and d) SJP printed device, respectively, with sonicated ink, and e) SJP printed device with unsonicated ink, for V_g varying from −16.0 to −2.0 V with a step of 2 V.

and drain electrodes.[81,82] In another study, a stick percolation model was employed to explain the device performance improvement from strip patterning.[79,80] This model deduced an increase of the SWCNT network percolation beyond the density of the metallic-SWCNTs (m-SWCNTs) in the device and eliminating current conduction purely through the m-SWCNT pathways.

Extracted mobility versus logarithmic I_{ON}/I_{OFF} is plotted in **Figure** 4a. The trend for IJP-printed CNT-TFT devices appears random, consistent with recent literature,[9] whereas SJP-printed devices follow the trend observed in synthesized random CNT network thin-film transistors.[76,78] Figure 4b,c illustrates the trends in mobility and the logarithm of the I_{ON}/I_{OFF}, respectively, under various printing conditions for increasing channel lengths, ranging from 2 to 300 µm, while the channel width is fixed at 300 µm. At different lengths, vertical bars show the range of respective data points, and mean values are connected for each printed device type. Unless otherwise specified, all the devices were fabricated with sonicated ink. While IJP showed minor increase in mobility with an increase in channel length similar to previously reported results,[83] there is not a definite trend for SJP printed devices below 100 µm. However, from 100 µm onward, mobility showed an increasing trend and SJP exhibits superior mobility for devices with a channel length of 300 µm, the maximum channel length used in this study. Although the mobility of SJP devices at 300 µm is better, the variability in terms of standard deviation is five times larger than IJP. Devices printed with

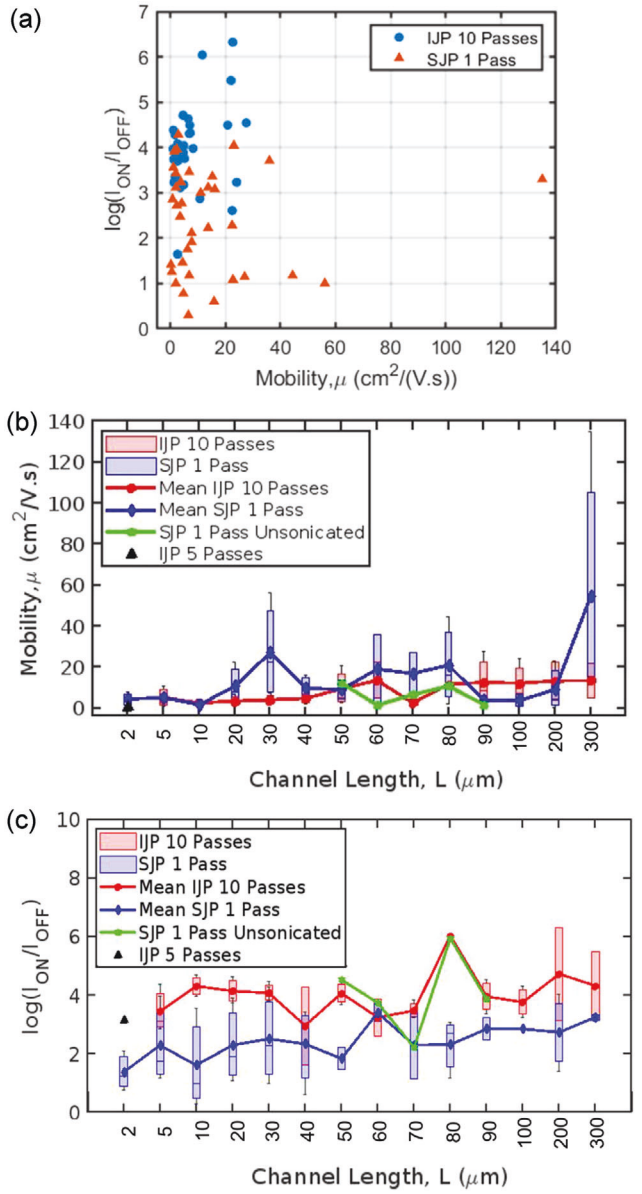

Figure 4. a) Transistor field-effect mobility with respect to I_{ON}/I_{OFF} for both printer types are overlayed showing different trend. b) Mobility and c) log (I_{ON}/I_{OFF}) vs Channel Length plot for IJP and SJP devices with and without ink sonication for different print passes. Here, inks are sonicated ink unless otherwise stated.

unsonicated ink follow a different trend of mobility versus channel length, varying between sonicated SJP and IJP printed devices. The I_{ON}/I_{OFF} versus channel length showed an increasing trend for IJP and a relatively flat response for SJP. Overall, within the printed channel length range of 2–300 µm, the I_{ON}/I_{OFF} versus channel length trend for IJP-printed CNT-TFTs outperforms that of SJP with sonicated ink. However, it's worth noting that unsonicated ink-printed SJP CNT-TFTs exhibit a trend that matches IJP, albeit with limited data points. The difference in the I_{ON}/I_{OFF} between sonicated and unsonicated ink-printed SJP CNT-TFTs may be attributed to clotted CNTs forming more CNT-CNT junctions in the CNT network of unsonicated ink compared to that of sonicated ink. Although SJP showed promising performance, the variability is more than IJP which could be improved by exploring ink formulation parameters, material-substrate interaction, pre- and post-print processing. Recently, AJP printed uniform CNT device performance was achieved by controlling the CNT ink bath temperature during printing, ink formulation with non-volatile and viscosifying additives, and a thermal treatment for polymer removal.[84]

4. Discussion

In this work, we address the challenges of ink sonication dependence and nozzle clogging associated with conventional printers, especially when dealing with stored 1D nanomaterial ink such as CNTs. In comparison, our nozzle-free, high-speed liquid micro jetting by SJP effectively addresses this issue. This innovative method offers several advantages. First, SJP widens the range of jettable materials in terms of nanomaterial dimensions. With the nozzle-free approach, inks containing particles or flakes comparable in size to or larger than typical nozzle widths can be used. Additionally, this acoustic approach frees one from choosing only optically transparent and thermally stable materials. Second, this jetting method is highly tolerant of variations in the position of the liquid surface within the acoustic focal length (several hundred µm), which enhances controllability even when factors such as evaporation and liquid consumption cause slight changes in the liquid level. Third, the absence of a nozzle and the reduction in sonication help minimize CNT damage, resulting in longer tube lengths. This has the potential to enhance device performance, reducing carrier scattering and improving current conduction.[85,86] Raman characterization also showed a similar D-peak for IJP and SJP (shown in Figure S5, Supporting information), confirming no unexpected change in the morphology of SJP printed CNTs. This is evidenced by the measured maximum effective mobility of ≈135 $cm^2\ V^{-1}\ s^{-1}$. Finally, SJP printing is expected to be more effective in ink material utilization, considering factors such as sonication, the number of printing passes required, and ink volume used, thanks to the reduced number of print passes.

In terms of device performance comparison between the two print modalities, SJP demonstrates promising electrical performance, even with a single printing pass and lower surface coverage. This can be attributed to the underlying printing mechanism in the SJP system, where high-speed liquid microjetting enables a significant volume of CNT ink deposition with better adhesion to the surface and the metal contacts compared to IJP. Similar pressure dependence on the deposition thickness was also demonstrated recently for plasma jet printer,[87] where increasing precursor flow resulted in an increase in the average film thickness. In contrast, IJP's smaller print volume (native drop volume 2.4 pL, individual dot size 30 µm) and varying adhesion after the first pass result in non-uniform adhesion from one layer to another (functionalized SiO_2 surface vs CNT and/or surfactant surface). Additionally, IJP-printed CNTs have shorter lengths, as observed in Figures 2a and 5a, making it challenging to form a good interface with source and drain metal with just one print pass for bottom contacted devices. Consequently, multiple IJP print passes are required to achieve electrical connectivity

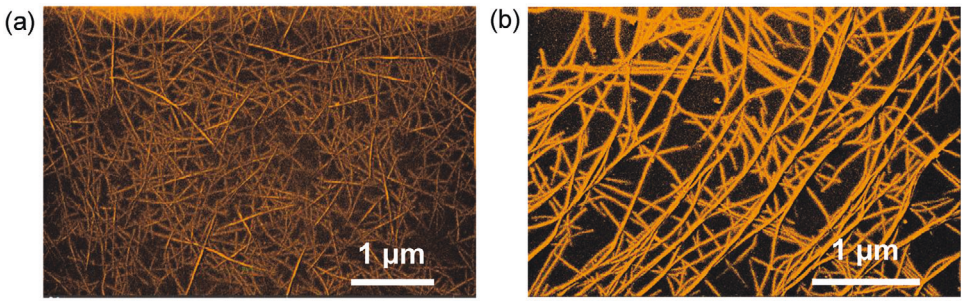

Figure 5. Zoomed in SEM of a) ten print pass IJP printed channel with high density CNTs and varying length, mostly smaller in dimension compared to b) one print pass SJP printed channel with lighter density but longer tube length. Scale bar is 1 µm for both cases. CNTs are false colored to highlight the difference.

of the individual CNT strands. Furthermore, CNTs are damaged during overall IJP printing process due to sonication and nozzle diameter, whereas SJP is not limited by these factors. This is clearly observed when comparing the zoomed-in SEM image of an IJP-printed CNT channel in Figure 5a to that of an SJP-printed CNT channel in Figure 5b. SJP-printed CNTs span the entire image in Figure 5b, whereas IJP-printed CNTs are broken and heavily rely on CNT-CNT junctions for electrical conduction between source and drain contacts. This also confirms that nozzle-free SJP can print CNTs with tube lengths covering the entire length histogram (Figure S1, Supporting information) of the commercially available CNT ink, minimizing the CNT damage and improving electrical performance. The experimental findings presented in this work hold significant promise for addressing challenges such as nozzle clogging and expanding the application space for random CNT network and other nanomaterial films in various fields, including microelectronics, nanoelectronics, optoelectronics, flexible electronics, sensors, radio frequency (RF) communications, photonics, and micro/nanoelectromechanical systems (M/N-EMS).[88]

5. Conclusion

In summary, we have successfully demonstrated the fabrication of printed CNT channel TFTs with good electrical performance using the nozzle-free SJP system. These devices were systematically compared with inkjet-printed CNT-TFTs, all with highly doped Si as a back-gate and SiO_2 as the gate dielectric. Notably, the IJP-printed channels required ten printing passes to achieve fully functional devices, especially for long channels. In stark contrast, the SJP system required only a single printing pass for comparable electrical characteristics. Morphological analysis revealed that SJP was capable of printing significantly longer tube lengths, spanning the entire commercially available CNT range. In contrast, IJP printing produced much smaller CNTs, strictly limited by the nozzle diameter. For stored ink, sonication was necessary to prevent nozzle-clogging in inkjet printing. However, the SJP system successfully printed functional devices with reasonable performance using stored ink, without any sonication. Furthermore, as the channel length is increased, the nozzle-free SJP system exhibited a more significant increase in mobility compared to inkjet technology, resulting in a six-fold higher optimal field effect mobility for the former system. Conversely, inkjet printing showed an increase in the I_{ON}/I_{OFF}, indicating the influence of CNT-CNT junctions on performance due to smaller tube lengths. In contrast, SJP printing with longer tube lengths maintained a relatively constant I_{ON}/I_{OFF} albeit at a lower magnitude compared to IJP. This difference is likely due to the longer tube lengths and fewer CNT-CNT junctions in lightly dense CNT networks achieved with SJP. SJP offers the advantage of no clogging, no ink sonication, fewer passes, and less damage to the CNTs. It enables longer CNT strands with fewer connections to bridge the source and drain electrode, imparting higher charge mobility. This study implies that nozzle-free printing method such as SJP is poised to handle ink materials that are difficult for traditional IJP.

6. Experimental Section

Photolithography and Metallization: The gold Source (S) and Drain (D) contacts were patterned on 90 nm SiO_2/Si using photolithography, physical vapor deposition-based metallization, and resist remover-based lift-off methodology. Subsequently, a commercially available aqueous solution of 99.9% pure semiconducting single-walled carbon nanotubes from NanoIntegris with a concentration of 0.01 mg mL^{-1} was utilized to print semiconducting channels in the device channel area to fabricate CNT transistors.

Substrate Cleaning: Before printing the channels, the substrates were cleaned with acetone, isopropyl alcohol (IPA), and DI water. Then the substrates were treated with oxygen plasma for 4 min at 100 W to remove any contaminants and to promote CNT adhesion to the SiO_2 surface. To further promote the CNT adhesion to the oxide surface, the substrates were then soaked in poly-L-Lysine solution (0.1% w/v in water) for 5 min and then swished in DI water.

Print Parameters: All inks used in this study for CNT printing with IJP and SJP were unfiltered. Fujifilm Dimatix Materials Printer DMP-2850 was used for inkjet printing of CNTs. Platen temperature was 60 °C, cartridge temperature was 40 °C; number of nozzles used for printing was 1, cartridge print height was 300 µm, jetting voltage was 30 V, jetting frequency was 1 KHz, drop spacing was 20 µm, printing speed was ≈10 mm $^{-1}$s and CNT ink concentration was 0.01 mg mL^{-1}. The IJP printed CNT density from SEM was 72 CNT μm^{-2}. The SJP system used a Nd:YAG laser with a 20 Hz pulse rate. The same NanoIntegris ink with CNT concentration 0.01 mg mL^{-1} was used in this system and placed above the PVD film on the water capsule. The ink height was adjusted until it was ≈10 microns above the focal point of the ultrasound. With evaporation and heating, this level slowly dropped. The substrate was lowered to keep the working distance near 250 microns. Once poor jetting was seen, the ink height was replenished. As a result, 20 × 500 micron ink jets were produced at 20 Hz, depositing ink drops onto the substrate. The ink was at room temperature and the substrate was heated to 60 °C. The substrate was translated at 50 µm s^{-1}. For SJP CNT density was 22 CNT μm^{-2}.

Printing and Annealing: Upon drying the substrates with the nitrogen gun, the substrates were installed onto the heated platen of the printers for printing the semiconducting channels. The platen temperature of the inkjet printer was kept at 60 °C (highest achievable temperature in DMP-2850) and at 80 °C for the SJP system during the entire printing process. Here, the highly doped Si serves as the back gate, with 90 nm SiO_2 as gate dielectric. After printing channels, the samples were kept on top of a hot plate at 80 °C undisturbed for 15 min and then dipped in DI water for 10 s at 80 °C under a fume hood to remove any proprietary surfactant present in the channel area, as the presence of any surfactants in the channel significantly compromised the device performance. After rinsing, the samples were put inside a tube furnace and annealed at 200 C in H_2/N_2 forming gas environment for 40 min. Once the samples cooled down after annealing, the devices were ready for electrical characterization.

Electrical Characterization: Transistor electrical characterizations were performed using a Keithley-4200 on probe station.

Morphological Characterization: SEM and AFM: A Field Emission Scanning Electron Microscope (FEI Teneo) under a high vacuum was used for imaging analysis. The ETD and T1 detectors were used to obtain varying resolutions in imaging the deposited material. Printed CNT was imaged using a Bruker Dimension Icon atomic force microscope (AFM) under atmospheric conditions. Imaging was performed using a ScanAsyst-Air probe (Bruker, 2 nm radius of curvature) operating in PeakForce Tapping mode.

Supporting Information

Supporting Information is available from the Wiley Online Library or from the author.

Acknowledgements

S.S. and B.R. contributed equally to this work. The authors would like to acknowledge the staff and students of the Surface Science Lab at Boise State University (BSU) for their advice and assistance in AFM imaging and analysis. SS acknowledges help and guidance from Tony Varghese, Department of Electrical and Computer Engineering, BSU, Cadré Francis, Micron School of Materials Science and Engineering, BSU, for helping in material characterization, and M Arif Malik, Computer Science Program, Boise State University, for surface coverage analysis Python scripting related discussion. Financial support for this work from the National Science Foundation (Award Number:1825502) is thankfully acknowledged. This work was also supported in part through the Department of Energy Advanced Sensors and Instrumentation program under DOE Idaho Operations Office Contract DE-AC07-05ID14517. The authors acknowledge infrastructure support from the Department of Energy Nuclear Science User Facilities General Infrastructure Program through award numbers DE-NE0008677 and DE-NE0008496. The views and opinions of the authors expressed herein do not necessarily state or reflect those of the U.S. Government or any agency thereof. The authors are also supported by the Center for Advanced Energy Studies, the Idaho Global Entrepreneurship Mission, the Micron Foundation, and the M. J. Murdock Charitable Trust. The material presented here also used infrastructure sponsored by Air Force Research Laboratory (AFRL) under Agreement Number FA8650-20-2-5506. The U.S. Government is authorized to reproduce and distribute reprints for Governmental Purposes notwithstanding any copyright notation thereon. BR and LJG also acknowledge support from NSF, through award number CMMI- 1825945, and College of Engineering at the University of Michigan for supporting the nanofabrication performed in the Lurie Nanofabrication Facility (LNF).

Conflict of Interest

The authors declare no conflict of interest.

Data Availability Statement

The data that support the findings of this study are available from the corresponding author upon reasonable request.

Keywords

carbon nanotubes, CNT, inkjet printing, laser-generated focused ultrasound, nozzle-free printing

Received: November 18, 2023
Revised: February 27, 2024
Published online:

[1] W. S. Wong, A. Salleo, *Flexible electronics: materials and applications*, Springer, New York **2009**.
[2] J. A. Rogers, T. Someya, Y. Huang, *Science* **2010**, *327*, 1603.
[3] A. C. Arias, J. D. MacKenzie, I. McCulloch, J. Rivnay, A. Salleo, *Chem. Rev.* **2010**, *110*, 3.
[4] M. L. Hammock, A. Chortos, B. C.-K. Tee, J. B.-H. Tok, Z. Bao, *Adv. Mater.* **2013**, *25*, 5997.
[5] A. Rae, iNEMI Roadmap 2017.
[6] Y. Khan, A. Thielens, S. Muin, J. Ting, C. Baumbauer, A. C. Arias, *Adv. Mater.* **2019**, *32*, 1905279.
[7] N. Manufacturing, https://www.nextflex.us/, **2024**.
[8] T. R. Ray, J. Choi, A. J. Bandodkar, S. Krishnan, P. Gutruf, L. Tian, R. Ghaffari, J. A. Rogers, *Chem. Rev.* **2019**, *119*, 5461.
[9] T. Starner, IEEE Micro, IEEE, **2001**, *21*, 44.
[10] Y. Lin, M. Bariya, A. Javey, *Adv. Funct. Mater.* **2020**, *31*, 2008087.
[11] H.-H. Xu, L. Yin, C. Liu, X. Sheng, N. Zhao, *Adv. Mater.* **2018**, *30*, 1800156.
[12] Y. Khan, A. E. Ostfeld, C. M. Lochner, A. Pierre, A. C. Arias, *Adv. Mater.* **2016**, *28*, 4373.
[13] S. F. Shaikh, H. F. Mazo-Mantilla, N. Qaiser, S. M. Khan, J. M. Nassar, N. R. Geraldi, C. M. Duarte, M. M. Hussain, *Small* **2019**, *15*, 1804385.
[14] A. Kamyshny, S. Magdassi, *Small* **2014**, *10*, 3515.
[15] T. Ge, Z. Jia, J. S. Chang, *2018 IEEE International Symposium on Circuits and Systems*, IEEE, Florence, Italy **2018**.
[16] D. R. Hackler, D. Sime, S. L. Wald, Proceedings of the IEEE 2015, IEEE, **2015**, *103*, 633.
[17] V. R. Marinov, *International Symposium on Microelectronics* **2017**, 2017.
[18] R. Herbert, J.-H. Kim, Y. Kim, H. Lee, W.-H. Yeo, *Materials* **2018**, *11*, 187.
[19] Y. Li, S. Nayak, Y. Luo, Y. Liu, K. Salila, J. Pan, Z. Liu, C.-H. Heng, A. Thean, *Materials* **2019**, *12*, 1458.
[20] Y. Ma, Y. Zhang, S. Cai, Z. Han, X. Liu, F. Wang, Y. Cao, Z. Wang, H. Li, Y. Chen, X. Feng, *Adv. Mater.* **2020**, *32*, 1902062.
[21] R. L. Chaney, D. Hackler, D. G. Wilson, B. N. Meek, *IEEE Workshop on Microelectronics and Electron Devices* **2014**, 1.
[22] A. I. Hussein, *12th Learning and Technology Conference*, IEEE, Jeddah, Saudi Arabia **2015**.
[23] V. Subramanian, J. B. Chang, Alejandro, D. Q. Hr, L. Jagannathan, F. Liao, B. A. Mattis, S. Molesa, D. R. Redinger, D. Soltman, S. K. Volkman, Q. Zhang, *European Solid-State Circuits Conference* **2008**, 17.
[24] S. R. Forrest, *Nature* **2004**, *428*, 911.
[25] S. Khan, L. Lorenzelli, R. S. Dahiya, *IEEE Sens. J.* **2015**, *15*, 3164.
[26] C. Yeom, K. Chen, D. Kiriya, Z. Yu, G. Cho, A. Javey, *Adv. Mater.* **2015**, *27*, 1561.
[27] S. Yao, Y. Zhu, *Nanoscale* **2014**, *6*, 2345.
[28] L. Li, L. Pan, Z. Ma, K. Yan, W. Cheng, Y. Shi, G. Yu, *Nano Lett.* **2018**, *18*, 3322.

[29] S. Harada, W. Honda, T. Arie, S. Akita, K. Takei, *A. C. S. Nano* **2014**, *8*, 3921.
[30] Y. Feng, L. Xie, Q. Chen, L.-R. Zheng, *IEEE Sens. J.* **2015**, *15*, 3201.
[31] J. Zuo, J. Feng, M. G. Gameiro, Y. Tian, J. Liang, Y. Wang, J. Ding, Q. He, *Future Foods* **2022**, *6*, 100198.
[32] J. B. Andrews, C. Cao, M. A. Brooke, A. D. Franklin, *IEEE Sens. J.* **2017**, *17*, 4612.
[33] Y. Yamamoto, S. Harada, D. Yamamoto, W. Honda, T. Arie, S. Akita, K. Takei, *Sci. Adv.* **2016**, *2*, 1601473.
[34] A. S. G. Reddy, B. B. Narakathu, M. Z. Atashbar, M. Rebros, E. Rebrosova, M. K. Joyce, *Proc. Eng.* **2011**, *25*, 120.
[35] S. K. Eshkalak, A. Chinnappan, W. A. D. M. Jayathilaka, M. Khatibzadeh, E. Kowsari, S. Ramakrishna, *Appl. Mater. Today* **2017**, *9*, 372.
[36] S. G. Bucella, J. M. Salazar-Rios, V. Derenskyi, M. Fritsch, U. Scherf, M. A. Loi, M. Caironi, *Adv. Electron. Mater.* **2016**, *2*, 1600094.
[37] K. D. Ausman, R. D. Piner, O. Lourie, R. S. Ruoff, M. V. Korobov, *J. Phys. Chem. B* **2000**, *104*, 8911.
[38] S.-P. Chen, J. R. Durán Retamal, D.-H. Lien, J.-H. He, Y.-C. Liao, *RSC Adv.* **2015**, *5*, 70707.
[39] C. Goth, S. Putzo, J. Franke, *IEEE 61st Electronic Components and Technology Conference*, IEEE, Lake Buena Vista, FL, USA **2011**.
[40] T. Lee, H. W. Baac, J. G. Ok, H. S. Youn, L. Jay Guo, *Phys. Rev.applied* **2015**, *3*, 044007.
[41] H. W. Baac, J. G. Ok, A. Maxwell, K.-T. Lee, Y.-C. Chen, A. J. Hart, Z. Xu, E. Yoon, L. J. Guo, *Sci. Rep.* **2012**, *2*, 989.
[42] D. Bucknall, *Nanolithography and Patterning Techniques in Microelectronics*, Elsevier, Amsterdam **2005**.
[43] W. S. Wong, E. M. Chow, R. Lujan, V. Geluz-Aguilar, M. L. Chabinyc, *Appl. Phys. Lett.* **2006**, *89*, 142118.
[44] H. Kipphan, *Handbook of Print Media: Technologies, and Production Methods*, Springer, Berlin, Heidelberg **2001**.
[45] V. Marinov, *International Journal of Adaptive Control and Signal Processing* **2005**, *19*, 741.
[46] B. Ballarin, A. Fraleoni-Morgera, D. Frascaro, S. Marazzita, C. Piana, L. Setti, *Synth. Met.* **2004**, *146*, 201.
[47] *FUJIFILM Dimatix Material Printer DMP-2800 Seriese User's Manual*, 2nd ed., FUJIFILM Dimatix, Inc., USA **2010**.
[48] D. B. Bogy, F. E. Talke, *IBM J. Res. Dev.* **1984**, *28*, 314.
[49] L. Hu, D. S. Hecht, G. Grüner, *Nano Lett.* **2004**, *4*, 2513.
[50] K. Schnittker, M. Tursunniyaz, J. B. Andrews, *J. Inf. Disp.* **2021**, *22*, 193.
[51] D. Corzo, K. Almasabi, E. Bihar, S. Macphee, D. Rosas-Villalva, N. Gasparini, S. Inal, D. Baran, *Adv. Mater. Technol.* **2019**, *4*, 1900040.
[52] J. Ebert, E. Ozkol, A. Zeichner, K. Uibel, O. Weiss, U. Koops, R. Telle, H. Fischer, *Journal of Dental Research* **2009**, *88*, 673.
[53] R. Tortorich, J.-W. Choi, *Nanomaterials* **2013**, *3*, 453.
[54] D. S. Hecht, L. Hu, G. Irvin, *Adv. Mater.* **2011**, *23*, 1482.
[55] Fujifilm, 'Dimatix Materials Cartridge - Samba Cartidge', https://asset.fujifilm.com/www/us/files/2021-04/ae8a1e167ce8c273fcdd31ecffd9ec80/PDS00142.pdf, **2021**.
[56] Fujifilm, 'Fujifilm Dimatix Materials Printer DMP-2800 Series User Manual', https://content.ilabsolutions.com/wp-content/uploads/2016/11/DMP-2800-Users-Guide-Version-2.0.6.pdf, **2008**.
[57] NanoIntegris, 'Semiconducting SWNTs (IsoNanotubes-S)' https://nanointegris.com/semiconducting-swnts-isonanotubes-s/, **2024**.
[58] G. Gao, T. Yonezawa, K. Hubbell, G. Dai, X. Cui, *Biotechnol. J.* **2015**, *10*, 1568.
[59] J. Perelaer, C. E. Hendriks, A. W. M. de Laat, U. S. Schubert, *Nanotechnology* **2009**, *20*, 165303.
[60] S. Sumaiya, K. Kardel, A. El-Shahat, *Technologies* **2017**, *5*, 53.
[61] S. Mitragotri, *Nat. Rev. Drug Discovery* **2006**, *5*, 543.
[62] S. Elrod, B. Hadimioglu, B. T. Khuri-Yakub, E. G. Rawson, E. A. Richley, C. F. Quate, N. N. Mansour, T. S. Lundgren, *J. Appl. Phys.* **1989**, *65*, 3441.
[63] S. T. Thoroddsen, K. Takehara, T. G. Etoh, C. Ohl, *Phys. Fluids* **2009**, *21*, 112101.
[64] A. Patrascioiu, J. M. Fernández-Pradas, J. L. Morenza, P. Serra, *Appl. Surf. Sci.* **2014**, *302*, 303.
[65] A. Patrascioiu, J. M. Fernández-Pradas, A. Palla-Papavlu, J. L. Morenza, P. Serra, *Microfluidics and Nanofluidics* **2013**, *16*, 55.
[66] K. Chen, W. Gao, S. Emaminejad, D. Kiriya, H. Ota, H. Y. Y. Nyein, K. Takei, A. Javey, *Adv. Mater.* **2016**, *28*, 4397.
[67] M. Singh, H. M. Haverinen, P. Dhagat, G. E. Jabbour, *Adv. Mater.* **2010**, *22*, 673.
[68] G. L. Goh, S. Agarwala, W. Y. Yeong, *ACS Appl. Mater. Interfaces* **2019**, *11*, 43719.
[69] Z. Cheng, C. Pang, P. Wang, S. T. Le, Y. Wu, D. Shahrjerdi, I. Radu, M. C. Lemme, L. Peng, X. Duan, Z. Chen, J. Appenzeller, S. J. Koester, E. Pop, A. D. Franklin, C. A. Richter, *Nat. Electron.* **2022**, *5*, 416.
[70] A. D. Franklin, M. C. Hersam, H.-S. P. Wong, *Science* **2022**, *378*, 726.
[71] D. Estrada, S. Dutta, A. Liao, E. Pop, *Nanotechnology* **2010**, *21*, 085702.
[72] Q. Cao, M. Xia, C. Kocabaş, M. Shim, J. Li, S. V. Rotkin, *Appl. Phys. Lett.* **2007**, *90*, 023516.
[73] Q. Cao, H. Kim, N. Pimparkar, J. P. Kulkarni, C. Wang, M. Shim, K. Roy, M. A. Alam, J. A. Rogers, *Nature* **2008**, *454*, 495.
[74] C. Wang, J.-C. Chien, K. Takei, T. Takahashi, J. Nah, A. M. Niknejad, A. Javey, *Nano Lett.* **2012**, *12*, 1527.
[75] D. Estrada, E. Pop, *Appl. Phys. Lett.* **2011**, *98*, 073102.
[76] M. Y. Timmermans, D. Estrada, A. G. Nasibulin, J. D. Wood, A. Behnam, D. Sun, Y. Ohno, J. W. Lyding, A. Hassanien, E. Pop, E. I. Kauppinen, *Nano Res.* **2012**, *5*, 307.
[77] F. Scuratti, J. M. Salazar-Rios, A. Luzio, S. Kowalski, S. Allard, S. Jung, U. Scherf, M. A. Loi, M. Caironi, *Adv. Funct. Mater.* **2020**, *31*, 2006895.
[78] S. J. Choi, P. Bennett, D. Lee, J. Bokor, *Nano Res.* **2015**, *8*, 1320.
[79] A. E. Islam, J. A. Rogers, M. A. Alam, *Adv. Mater.* **2015**, *27*, 7908.
[80] N. Pimparkar, Q. Cao, J. A. Rogers, M. A. Alam, *Nano Res.* **2019**, *2*, 167.
[81] B. K. Sarker, S. Shekhar, S. I. Khondaker, *ACS Nano* **2011**, *5*, 6297.
[82] C. Wang, J. Zhang, K. Ryu, A. Badmaev, L. Gomez, C. Zhou, *Nano Lett.* **2009**, *9*, 4285.
[83] N. Rouhi, D. Jain, K. Zand, P. Burke, *Adv. Mater.* **2011**, *23*, 94.
[84] S. Lu, J. Zheng, J. A. Cardenas, N. X. Williams, Y. C. Lin, A. D. Franklin, *ACS Appl. Mater. Interfaces* **2020**, *12*, 43083.
[85] D. Hecht, L. Hu, G. Grüner, *Appl. Phys. Lett.* **2006**, 89.
[86] S. P. Schießl, X. D. Vries, M. Rother, A. Massé, M. Brohmann, P. A. Bobbert, J. Zaumseil, *Phys. Rev. Mater.* **2017**, *1*, 046003.
[87] J. Manzi, A. E. Weltner, T. Varghese, N. McKibben, M. Busuladzic-Begic, D. Estrada, H. Subbaraman, *Nanoscale* **2023**, *15*, 6596.
[88] M.-H. Seo, J.-Y. Yoo, M.-S. Jo, J.-B. Yoon, *Adv. Mater.* **2020**, *32*, 1907082.

